Networks and Heterogeneous Media

https://www.aimspress.com/journal/nhm

NHM, 21(2): 531–550.
DOI: 10.3934/nhm.2026024
Received: 04 November 2025
Revised: 10 March 2026
Accepted: 20 March 2026
Published: 31 March 2026

Research article

A superconvergent multiscale scheme for the Helmholtz equation in rapidly oscillating heterogeneous media

Shan Jiang[1,*], **Weipeng Miao**[1], **Huayi Wei**[2] **and Nianyu Yi**[2]

[1] School of Mathematics and Statistics, Nantong University, Nantong 226019, China
[2] School of Mathematics and Computational Science, Xiangtan University, Xiangtan 411105, China

* **Correspondence:** Email: jiangshan@ntu.edu.cn.

Abstract: We present a superconvergent and highly efficient multiscale finite element scheme for solving the Helmholtz equation in heterogeneous media. The proposed scheme is specifically designed to address the challenges posed by the multiscale nature of the Helmholtz equation, which often leads to high computational costs and numerical instabilities in traditional methods. By constructing tailored multiscale basis functions, the proposed approach effectively captures both the local fine-scale features and global macroscale behaviors of the multiscale solution. The fundamental mechanism underlying the multiscale scheme is systematically expounded. Through rigorous error analyses, we derive a second-order superconvergence result in the H^1 norm. Additionally, numerical experiments are conducted to validate the performance of the scheme. Both theoretical findings and numerical results confirm that the proposed multiscale scheme not only achieves higher solution accuracy but also exhibits superconvergence rates and significantly reduces computational costs.

Keywords: Helmholtz equation; multiscale finite element method; multiscale decomposition; H^1 norm; superconvergence

1. Introduction

The Helmholtz equation, a fundamental partial differential equation (PDE) plays a pivotal role in various scientific and engineering fields. In acoustics, it is used to model the propagation of sound waves, enabling the design and analysis of sound-absorbing materials and noise control systems. In electromagnetics, it describes the behavior of electromagnetic waves. In seismology, the Helmholtz equation helps in understanding the propagation of seismic waves through the Earth's crust, aiding in earthquake prediction and oil exploration.

Traditionally, numerical methods such as the finite element method (FEM) have been employed to solve the Helmholtz equation. However, these methods face significant challenges. The Helmholtz

equation often exhibits multiscale features, where the solution varies over a wide range of length scales. Standard FEM demands an extremely fine mesh for accurate resolution of all these scales, resulting in an excessively large number of degrees of freedom. This not only exponentially increases the computational cost but also may cause numerical instabilities, especially in high oscillation heterogeneous media.

The multiscale finite element method (MsFEM) has emerged in recent years as a compelling alternative, designed to surmount the limitations of traditional numerical approaches. Its core aim is to address two key drawbacks: The prohibitive computational costs that escalate with mesh density, and the numerical instabilities closely tied to heterogeneous media. These issues often hinder traditional methods when dealing with large-scale simulations or high oscillation problems, which are common in real-world engineering applications. Unlike conventional approaches, which struggle to balance accuracy and efficiency in multiscale scenarios, MsFEM is specifically designed to capture the complex multiscale behavior of solutions without relying on the computationally unfeasible global fine meshes required by standard FEM. Its key strength lies in a novel strategy for constructing local multiscale basis functions, which effectively approximate solution features across both micro- and macro-scales. These basis functions are tailored to embed critical small-scale details (e.g., local oscillations) while operating with far greater efficiency than their standard FEM counterparts. By confining fine-scale resolution to local subdomains rather than the entire computational domain, MsFEM avoids the exponential surge in degrees of freedom that plagues traditional methods, preserving high accuracy while drastically reducing computational burdens in practical use.

The study of the Helmholtz equation has a long history, as shown in [1–3]. Ihlenburg and Babuska [1] pioneered addressing the h-version FEM to a 1D Helmholtz model, analyzed stability and errors, and found that when k^2h was small, H^1-norm error matched best approximation; for moderate–high wavenumbers, pollution error dominated. Oberai and Pinsky [2] first applied the multiscale finite element method to the Helmholtz equation, creating a local model where fine scales were incorporated analytically using Green's functions. Gallistl et al. [4] proposed a stable multiscale Petrov–Galerkin finite element method, and Jiang et al. [5] developed an adapted Petrov–Galerkin scheme, each for their specific applications. Later, in [6, 7], the multiscale hybrid–mixed method was introduced for the Helmholtz equation in heterogeneous domains. In [8], a heterogeneous multiscale method (HMM) for the Helmholtz equation with high contrast was proposed. However, the explicit stability estimate presented in Theorem 3.9 of that study led to a "worst case" resolution condition, where $k^5(H + h)$ had to be sufficiently small. This rendered the method computationally intensive, as it demanded extremely fine meshes (i.e., small values of H and h), particularly when dealing with high wavenumbers k. Chung et al. [9] and Fu et al. [10, 11] studied the generalized multiscale finite element method (GMsFEM) and the wavelet-based edge multiscale finite element method for Helmholtz problems. By using multiscale basis functions in acoustic media, they reduced the dimension of the discrete system and computational time, achieving convergent results under certain conditions.

On the other hand, high-order finite difference schemes and compact schemes were proposed in [12–14]. In these compact sixth-order schemes, a refined choice strategy based on minimizing numerical dispersion was developed for selecting weight parameters, and corresponding theoretical analyses were presented. The high accuracy and efficiency of the proposed schemes were demonstrated through numerous numerical experiments.

Many new studies on Helmholtz problems have emerged recently, as seen in [15–17]. For example, Jiang et al. [15] presented an efficient multiscale finite difference frequency-domain method for the

scalar Helmholtz equation. However, this method faced difficulties in dispersion analysis and insufficiently considered wave attenuation. Kalachikova et al. [16] investigated the GMsFEM for scattering problems in heterogeneous media. Freese et al. [17] studied high-frequency Helmholtz problems using superlocalized orthogonal decomposition (SLOD), achieving the superexponential decay of localization errors and a relaxed oversampling condition. Jiang et al. [18, 19] proposed a balanced truncation based on the generalized multiscale finite element method (BT-GMsFEM) for parameter-dependent elliptic and parabolic problems, respectively. In [20–22], Chen, Hou, and Wang made contributions to exponentially convergent multiscale methods (ExpMsFEM). Their initial work [20] broke new ground by achieving exponential convergence for multiscale linear elliptic PDEs, setting a new accuracy standard. They then extended this transformative approach to 2D high-frequency heterogeneous Helmholtz equations [21], addressing a critical problem in wave propagation. Their work [22] established a general and elegant multiscale finite element framework, unifying their previous results and providing a robust theoretical foundation for future research. Jiang et al. [23] used a multiscale scheme, and Cheng et al. [24, 25] applied the local discontinuous Galerkin method (LDG) to the singularly perturbed convection–diffusion and reaction–diffusion problems, achieving parameter-uniform superconvergence and supercloseness in these studies. A generalized finite element method with optimal local approximation was proposed in [26], and an extension of the approximate component mode synthesis was proposed in [27] for the heterogeneous Helmholtz equation, respectively. Saini et al. [28] developed a parameter-uniform higher order numerical scheme for the Robin-type parabolic reaction–diffusion problem with a large delay. In [29], the authors employed a variational formulation and fitted mesh discretization (3- or 5-point schemes, M-matrix transformation) to study reaction–diffusion problems on a k-star graph, achieving almost second-order uniform convergence, and validating the results numerically. Li and Wu [30] proposed higher-order FEM and continuous inner penalty finite element method (CIP-FEM) for the problem with high wave number and perfectly matched layer (PML) truncation; in their study, the presented estimation framework was generalized to Helmholtz PML problems with general scatterers. Bernkopf et al. [31] conducted a wavenumber-explicit stability and convergence analysis of hp finite element discretizations for Helmholtz problems in piecewise smooth media, providing a rigorous theoretical foundation for high-order methods applied to such heterogeneous settings. These numerical methods, each with their own advantages and limitations, have been crucial in exploring the intricate behavior of heterogeneous media.

This study distinguishes itself through the following key features: First, we propose a tailored multiscale finite element scheme for the Helmholtz equation in rapidly oscillating heterogeneous media, which leverages scale decomposition to construct efficient multiscale basis functions that accurately capture local fine-scale features while ensuring high-precision results. Second, we enhance the scheme's stability through a specialized data structure, where a mapping matrix efficiently reduces the coupling between macroscale and microscale basis functions to achieve economical computational complexity. Third, we establish a second-order superconvergence result in the H^1 norm via a systematic error analysis that explicitly accounts for the qualitative dependence of constants on the wavenumber and medium heterogeneity; this framework ensures the scheme's reliability and efficiency for multiscale Helmholtz problems in heterogeneous media.

The paper is organized as follows. In Section 2, the Helmholtz problem and its scale decompositions are introduced. In Section 3, the finite element method and the multiscale strategy are applied; here,

the mechanism and computing costs of the multiscale scheme are elaborated in detail. Subsequently, superconvergence is achieved through error analysis in Section 4. To verify the effectiveness of the MsFEM, numerical experiments are conducted and comparative analyses are performed in Section 5. Finally, Section 6 presents concluding remarks to summarize this study.

2. Model problem

We study a two-dimensional Helmholtz equation to solve for $u : \Omega \to \mathbb{C}$ from

$$\begin{cases} -\nabla^2 u - k^2 u = f & \text{in } \Omega, \\ u = g & \text{on } \Gamma, \end{cases} \tag{2.1}$$

where k denotes the variable wave number, $f : \Omega \to \mathbb{C}$ is the given forcing function, and $g : \Gamma \to \mathbb{C}$ represents the prescribed Dirichlet boundary data. To ensure the well-posedness of the continuous problem, we impose the key assumption that the wavenumber k is not an eigenvalue of the negative Laplacian operator $-\nabla^2$ with Dirichlet boundary conditions. Mathematically, this means $k^2 \notin \sigma(-\nabla^2; H_0^1(\Omega))$, where $\sigma(-\nabla^2; H_0^1(\Omega))$ denotes the spectrum of $-\nabla^2$ under the specified boundary conditions. This condition guarantees the existence and uniqueness of the solution $u \in H^1(\Omega)$ for any $f \in L^2(\Omega)$ and $g \in H^{1/2}(\Gamma)$. In heterogeneous media, the solution u in our study tends to exhibit rapid oscillations. This stems from sharp microscale variations in material properties (e.g., density, wave speed), which induce high-frequency fluctuations in the solution of the Helmholtz equation.

The weak formulation of Eq (2.1) is to find $u \in U$ such that

$$a(u, v) = (f, v), \quad \forall v \in V, \tag{2.2}$$

where the function spaces U and V are defined as

$$U = \left\{ u \mid u \in H^1(\Omega), \ \ u = g \ \text{ on } \Gamma \right\},$$

$$V = \left\{ v \mid v \in H^1(\Omega), \ \ v = 0 \ \text{ on } \Gamma \right\},$$

and the bilinear form $a(\cdot, \cdot) : U \times V \to \mathbb{C}$ is defined as

$$a(u, v) = (\nabla u, \nabla v) - k^2 (u, v), \tag{2.3}$$

and the inner products $(\cdot, \cdot)$ are defined as

$$(f, v) = \int_\Omega f v \, \mathrm{d}\Omega.$$

To establish the well-posedness of the discrete scheme, we adopt the continuity and coercivity analysis framework for sesquilinear forms. For a general numerical method, we consider a discrete solution space V^h (not necessarily a finite element space) and a discrete sesquilinear form $a_h(\cdot, \cdot)$ defined on $V^h \times V^h$. The key boundedness and coercivity properties are as follows:

$$\begin{aligned} |a_h(v_h, w_h)| &\leq C \|v_h\|_{1,h} \|w_h\|_{1,h}, \\ \operatorname{Re} a_h(v_h, v_h) &\geq \frac{1}{2} \|\nabla v_h\|^2_{L^2(\Omega)}, \end{aligned}$$

where $C > 0$ is a bounded constant, and $\|\cdot\|_{1,h}$ denotes a suitable mesh-dependent norm on V^h (e.g., a discrete H^1-like norm). The above coercivity estimate holds, which shows that the discrete sesquilinear form is coercive.

To ensure the stability of our numerical analysis, we restrict our study to the case of Helmholtz problems with absorption. This corresponds to a complex wavenumber $k \in \mathbb{C}$ with a positive imaginary part, that is, $k = k_r + \mathrm{i}k_i$, where $\mathrm{i} = \sqrt{-1}$, and $k_i > 0$. In this setting, the associated sesquilinear form becomes coercive on the space $H_0^1(\Omega)$. This crucial assumption is stated here and is used throughout the paper.

Then we consider the decomposition of u and v, that is, $u = u_0 + u_1$, $v = v_0 + v_1$, where u_0 and v_0 represent the resolvable scale part, and u_1 and v_1 represent the unresolvable scale part. Therefore, the weak formulation (2.2) can be expressed as

$$a(u_0 + u_1, v_0 + v_1) = (f, v_0 + v_1).$$

It leads to two subproblems as follows:

$$a(u_0, v_0) + a(u_1, v_0) = (f, v_0)$$

and

$$a(u_0, v_1) + a(u_1, v_1) = (f, v_1).$$

To fully capitalize on the unique scale-decomposition property of the Helmholtz problem, we can delve deeper into the design principles and implementation details of the multiscale strategy in the subsequent theoretical analysis. By focusing on how this decomposition mitigates scale-related numerical challenges (e.g., high-frequency oscillations), this approach may not only offer new insights into the problem's intrinsic structure but also significantly enhance the computational efficiency and accuracy of our research.

3. Multiscale strategy

3.1. Finite element method

When dealing with the weak formulation (2.2), we are faced with an infinite-dimensional problem. To overcome this challenge, it is crucial to employ appropriate numerical strategies to obtain a finite-dimensional approximation. In the context of the standard finite element method, we denote $\mathcal{T}^h$ as a fine-grained partition of the domain Ω into individual elements. For every element $K \in \mathcal{T}^h$, the size of the element satisfies the condition $0 < h_K << 1$. We define h as the maximum value among all h_K, that is, $h = \max_K h_K$. Inside each such fine-scale element K, a set of nodal basis functions is defined, which are associated with the four nodes of a rectangular element within the discretization framework.

The finite element space is constructed using piecewise bilinear polynomials $\mathbb{Q}^1(K)$ and is expressed as

$$V^h = \{v_h \in H^1(\Omega) : \ v_{h|_K} \in \mathbb{Q}^1(K), \ \forall K \in \mathcal{T}^h\}. \tag{3.1}$$

The Galerkin scheme aims to find $u_g \in V^h$ such that

$$a(u_g, v) = (f, v), \quad \forall v \in V_0^h. \tag{3.2}$$

Here, u_g represents the Galerkin FEM solution, which can be written as

$$u_g = \sum_{i}^{gb1} u_i \psi_i, \tag{3.3}$$

where ψ_i are the finite element basis functions, and $gb1$ denotes the number of global basis functions in the FEM.

In this method, let NM represent the number of fine-scale elements in the x and y directions, respectively. For two-dimensional problems, the total number of elements at the fine-mesh level is N^2M^2. It is well-known that the computational cost of the finite element method is of the order $O(N^2M^2)$.

3.2. Multiscale finite element method

In contrast to the finite element method, the multiscale finite element method begins by solving local problems for the multiscale basis functions φ_i. First, the domain Ω is divided into N^2 coarse elements in two dimensions (where N is the number of partitions along both the x- and y- directions). Within the framework of the multiscale finite element method, $\mathcal{T}^H$ denotes a coarse-grained partition of the domain into individual coarse elements. Then, for each coarse element K, we solve

$$\begin{cases} -\nabla^2 \varphi_i - k^2 \varphi_i = 0 & \text{in } K, \\ \varphi_i = \theta_i & \text{on } \partial K, \end{cases} \tag{3.4}$$

where ∂K denotes the entire boundary of element K. Given the specified boundary conditions (e.g., θ_i), the local problem (3.4) can be solved via the FEM with a subelement size of $h = H_K/M$, where H_K is the size of coarse element satisfying $H_K >> h$, and M is the number of subpartitions along each spatial direction.

Once the multiscale basis functions are obtained, the multiscale space U^H is generated as follows:

$$U^H = \text{span}\{\varphi_i : \ i = 1, \cdots, 4, \ \forall K \in \mathcal{T}^H\}. \tag{3.5}$$

With this approach, the multiscale basis functions are able to capture the microscopic details of the macroscopic problem (2.1), such as those related to acoustics and electromagnetic waves. Consequently, small-scale characteristics can be incorporated into the macroscopic solution. This implies that the multiscale basis functions have the flexibility to accommodate sufficient microscopic information and play a vital role in accurately representing the behavior of the problem as a whole across multiple scales.

The weak formulation of the multiscale strategy seeks to restrict the solution of Eq (2.2) to a finite-dimensional multiscale subspace U^H, where $U^H \subset H^1(\Omega)$. Specifically, we aim to find $u_H \in U^H$ such that

$$a(u_H, v) = (f, v), \quad \forall v \in U^H. \tag{3.6}$$

Here, u_H is the multiscale solution, which can be expressed as

$$u_H = \sum_{i}^{gb2} u_i \varphi_i, \tag{3.7}$$

where $gb2$ denotes the number of global multiscale basis functions in the MsFEM, in contrast to the aforementioned $gb1$ in the FEM (see Eq (3.3)). Note that $O(N^2) = gb2 << gb1 = O(N^2M^2)$. This

indicates that the multiscale scheme requires far fewer degrees of freedom (DOFs) than the traditional finite element scheme. Consequently, this significant reduction in complexity directly translates to a substantial saving in computational costs, confirming that the multiscale scheme outperforms the finite element scheme in terms of both DOFs efficiency and computational economy. We will provide the detailed data structure in what follows.

To explain the mechanism of the multiscale strategy in greater detail, we construct an enriched mapping matrix for the multiscale basis functions. We start with a coarse element $K_{i,j} = [x_i, x_{i+1}] \times [y_j, y_{j+1}]$. In the x-direction, there are $M + 1$ fine mesh nodes as

$$x_i = x_{i,1} < x_{i,2} < \cdots < x_{i,M+1} = x_{i+1}.$$

The distance between consecutive nodes satisfies

$$x_{i,k+1} - x_{i,k} = \frac{x_{i+1} - x_i}{M}, \quad k = 1, \cdots, M.$$

Similarly, in the y-direction, the fine mesh nodes $y_{j,k}$ follow an analogous pattern. Subsequently, the multiscale basis functions φ_i can be represented in the form

$$\varphi_i = \sum_{l=1}^{(M+1)^2} r_{il}\psi_l, \quad \varphi_j = \sum_{n=1}^{(M+1)^2} r_{jn}\psi_n, \tag{3.8}$$

where ψ_l and ψ_n are the standard finite element basis functions. The coefficients r_{il} and r_{jn} represent the combination coefficients between these two types of basis functions and are stored as elements of a global mapping matrix.

Let the global mapping matrix be denoted as $R = (r_{ij})$, where $i = 1, 2, \cdots, N_c$, and $j = 1, 2, \cdots, N_f$. Here, $N_c = (N_{\text{MsFEM}} + 1)^2$ and $N_f = (N_{\text{FEM}} + 1)^2$, with N_{MsFEM} denote the number of coarse-element partitions in the MsFEM, and N_{FEM} represents the number of fine-element partitions in the FEM. For typical multiscale problems, $N_f \gg N_c$ holds, which reflects the higher resolution of the fine grid relative to the coarse grid.

To facilitate subsequent algebraic operations (e.g., matrix assembly or linear system solving), the key relationship can be rewritten in a compact matrix form. This matrix representation not only simplifies the mathematical expression of the coupling between scales but also aligns with the computational framework of the finite element method.

Specifically, the matrix-form equivalent of formula (3.8) is given by

$$\Phi = R\Psi, \tag{3.9}$$

where $\Phi \in \mathbb{C}^{N_c \times 1}$ denotes the coarse-scale vector, collecting the discrete values of the coarse-scale component at all coarse-grid nodes; $\Psi \in \mathbb{C}^{N_f \times 1}$ represents the fine-scale vector, gathering the discrete values of the fine-scale component at all fine-grid nodes; and $R \in \mathbb{C}^{N_c \times N_f}$ is the global mapping matrix defined earlier. Its entries encode the linear coupling relationships between the fine-scale basis functions and coarse-scale basis functions, enabling the extraction of the coarse-scale vector Φ from the fine-scale vector Ψ via the matrix-vector multiplication in Eq (3.9).

It is reasonable to anticipate that as the macroscale partition number N (corresponding to N_{MsFEM}) and microscale partition number M (related to N_{FEM}) are refined simultaneously, the size of R will grow

accordingly. This is because the matrix inherently encodes requisite local multiscale information, and this information specifically refers to the coupling relationships between macro- and micro-scale basis functions across all subdomains.

Regarding the global stiffness matrix in the multiscale scheme, it is denoted as $A^c = (a_{ij}^c) = (a(\varphi_i, \varphi_j))$ in Eq (2.3), where the superscript c indicates the coarse-scale case. Together with the representation of multiscale basis functions given in Eq (3.8), the global elements are assembled from the following expression:

$$a_{ij}^c = \sum_{l=1}^{(M+1)^2} \sum_{n=1}^{(M+1)^2} r_{il} r_{jn} \int_K \left(\nabla \psi_l \cdot \nabla \psi_n - k^2 \psi_l \psi_n \right) \mathrm{d}K, \tag{3.10}$$

where $i, j = 1, 2, \cdots, (N_{\mathrm{MsFEM}} + 1)^2$. It should be noted that in the context where $N_{\mathrm{MsFEM}} = N$, its value is relatively small.

On the other hand, for the finite element scheme, we have $A^f = (a_{ij}^f) = (a(\psi_i, \psi_j))$, where the superscript f represents the fine-scale case. Here, $i, j = 1, 2, \cdots, (N_{\mathrm{FEM}} + 1)^2$. Note that in this case, when $N_{\mathrm{FEM}} = NM$, its value is relatively large. In a two-dimensional problem, the computational cost at this square level can be extremely high.

Now, let us demonstrate the relationship between these two strategies:

$$A^c = R A^f R^T.$$

In our code implementation, the rows and columns of the mapping matrix R inherently incorporate sufficient microscopic information within each macroscopic element K. As a consequence, a reduced matrix A^c and a reduced vector,

$$F^c = R F^f,$$

are both stored at the coarse scale to save computational resources. In the multiscale scheme, we assemble the global system to solve for u_H as follows:

$$A^c u_H = F^c. \tag{3.11}$$

Conversely, when the finite element method is applied to a very fine mesh, the resulting global system becomes significantly larger:

$$A^f u_g = F^f. \tag{3.12}$$

It is worth emphasizing that the fundamental distinction between FEM and MsFEM lies in the construction of their basis functions—a difference manifested in the form of the mapping matrix R. Traditional finite element methods typically employ linear or higher-order basis functions to span the functional space. In contrast, the multiscale finite element method proposed herein utilizes linear multiscale basis functions, which enable the computation of coarse-scale solutions within a space spanned by independently computed multiscale basis functions. This approach inherently facilitates the reconstruction of a functional space that enriches the representation at the coarse scale, rendering the multiscale finite element method a robust and efficient alternative to traditional approaches.

3.3. Computing cost advantages

In practical applications, the MsFEM stands out by offering significant advantages in both computational efficiency and solution accuracy. To quantify these advantages clearly, as defined above, we clarify the discretization parameters: let N denote the number of coarse-element partitions along each spatial direction in the macroscale computational domain, and let M represent the number of fine-element subpartitions within each coarse element, also along each direction. Under this partitioning framework, the total number of fine-grid elements covering the entire domain amounts to $(NM)^2$, as each coarse element is further divided into M^2 fine elements, and there are N^2 coarse elements in total.

For the traditional FEM, which relies on a uniform fine-grid discretization to capture both macroscale and microscale features, its computational complexity and memory requirements for storing large-scale matrices both scale as $O(N^2M^2)$. This quadratic dependence on the microscale partition number M becomes a major limitation in practice, especially when high microscale resolution is needed to model intricate details. Traditional FEM offers no separation between preprocessing and core solution phases, meaning this high complexity is incurred for every solve, even for parametric or time-dependent problems with identical microscale geometries.

In sharp contrast, MsFEM circumvents this bottleneck by decoupling the computational workflow into offline and online phases, a critical distinction for its practical efficiency. The offline phase incurs a one-time cost of $O(N^2M^2)$, which covers solving local fine-scale problems (scaling as $O(M^2)$ per coarse element) for all N^2 coarse elements and constructing the multiscale basis functions. Additionally, the global mapping matrix that links local fine-scale basis information to the coarse-scale solution space is assembled and stored during this offline stage. The online phase, by contrast, is drastically optimized: the coarse-scale solve scales as $O(N^2 + M^2)$, as the precomputed basis functions and global mapping matrix are reused directly, eliminating the need for fine-grid computations during the core solution process.

Crucially, this reduction in online computational burden does not come at the expense of accuracy. MsFEM's local multiscale basis functions are designed to retain key microscale behaviors, ensuring solutions remain comparable to traditional fine-grid FEM. This offline-online decomposition makes MsFEM well-suited for large-scale simulations with fixed microscale geometry, as the upfront offline cost is distributed across multiple online solves, yielding significant overall savings.

In Section 5, we will present detailed CPU time and memory usage measurements to validate the efficiency and accuracy performance of MsFEM against traditional FEM.

4. Superconvergence analyses

Let $\kappa(\mathbf{x})$ denote the medium heterogeneity with $\kappa_{\min} \leq \kappa(\mathbf{x}) \leq \kappa_{\max}$, and let all generic positive constants C and C_i be explicitly annotated to depend on k and κ (but not on the coarse mesh size H and the fine mesh size h). We also introduce the projection operator $\Pi_H : H_0^1(\Omega) \to U^H$ tailored to the local structure of κ and k for the heterogeneous Helmholtz equation and $u_I \in V^h$, the standard piecewise linear nodal interpolant of the exact solution u. We assume the exact solution is sufficiently regular: $u \in H^3(\Omega) \cap H_0^1(\Omega)$. The small parameter δ represents the local error committed in solving the fine-scale local problems, which we assume can be controlled such that $\delta = O(h^2)$.

Lemma 4.1. For any coarse element $K \in \mathcal{T}^H$, the $H^1(K)$ error between the exact solution u and its

multiscale interpolant $\Pi_H u$ satisfies

$$\|u - \Pi_H u\|_{H^1(K)} \leq C_1(k,\kappa)H|u|_{H^2(K)} + C_2(k)\delta, \tag{4.1}$$

where $|u|_{H^2(K)}$ is the seminorm of u in $H^2(K)$, and $\delta = O(h^2)$ is the local fine-scale discretization error.

Proof. We know that the multiscale basis functions are tailored to the local structure of the differential operator in Eq (3.4). The error is decomposed into the error due to the standard finite element interpolant and the error due to the local fine-scale solving. The first term is standard and yields $O(H)$. The second term, under the assumption that the local problems are solved with high accuracy $O(h^2)$, is of higher-order and can be absorbed into the constant for the final estimate.

Lemma 4.2. The global $H^1(\Omega)$ error between the multiscale interpolant and the standard linear interpolant is bounded by

$$\|\Pi_H u - u_I\|_{H^1(\Omega)} \leq C(k,\kappa)H^2|u|_{H^3(\Omega)}. \tag{4.2}$$

Proof. A careful analysis of the local problems (3.4), using Taylor expansion and the property that the multiscale basis functions (which quantify the improvement over the standard basis functions) satisfy the homogeneous Helmholtz equation locally, reveals that the dominant error terms cancel out, leaving a residual of order $O(H^2)$. The detailed proof proceeds as follows:

Because $\Pi_H u = \sum_i u_i\varphi_i$, $I_h u = u_I = \sum_i u_i\psi_i$, it follows that $\Pi_H u - u_I = \sum_i u_i(\varphi_i - \psi_i)$. Denote $\eta_i = \varphi_i - \psi_i$ for the heterogeneous Helmholtz equation so that η_i satisfies the local Helmholtz equation on K:

$$-\nabla^2\eta_i - k^2\eta_i = \nabla^2\psi_i + k^2\psi_i \text{ in } K.$$

Using the Taylor expansion of $u \in H^3(\Omega)$ at the nodal points $\mathbf{x}_j \in K$, we have

$$(\Pi_H u - u_I)|_K = \sum_i u(\mathbf{x}_i)\,\eta_i \approx$$

$$\sum_i \left[u\left(\mathbf{x}_j\right) + \nabla u\left(\mathbf{x}_j\right)\cdot\left(\mathbf{x}_i - \mathbf{x}_j\right) + \frac{1}{2}\left(\mathbf{x}_i - \mathbf{x}_j\right)^T D^2 u\left(\mathbf{x}_j\right)\left(\mathbf{x}_i - \mathbf{x}_j\right) + O\left(\left|\mathbf{x}_i - \mathbf{x}_j\right|^3\right)\right]\eta_i(\mathbf{x}).$$

The cubic term vanishes for $u \in H^3(\Omega)$, leaving a quadratic residual in H. By the Bramble–Hilbert lemma, it has

$$\|\eta_i\|_{H^1(K)} \leq C(k,\kappa)H\left\|\nabla^2\psi_i + k^2\psi_i\right\|_{L^\infty(K)}.$$

From the Helmholtz-adapted interpolation error estimate and the local error estimate, it follows that

$$\begin{aligned}
\|\Pi_H u - u_I\|_{H^1(K)} &\leq C(k,\kappa)H\,|\Pi_H u - u_I|_{H^2(K)}, \\
\|\Pi_H u - u_I\|_{L^2(K)} &\leq C(k,\kappa)H^2|u|_{H^3(K)}, \\
\|\nabla(\Pi_H u - u_I)\|_{L^2(K)} &\leq C(k,\kappa)H^2|u|_{H^3(K)}.
\end{aligned}$$

Summing over all local coarse elements of the domain yields the global $H^1(\Omega)$ estimate:

$$\begin{aligned}
\|\Pi_H u - u_I\|^2_{H^1(\Omega)} &= \sum_K \|\Pi_H u - u_I\|^2_{H^1(K)} \\
&\leq \sum_K C(k,\kappa)H^4|u|^2_{H^3(K)} \leq C(k,\kappa)H^4|u|^2_{H^3(\Omega)}.
\end{aligned}$$

Lemma 4.3. The global $H^1(\Omega)$ error between the standard linear interpolant and the multiscale solution is bounded by

$$\|u_I - u_H\|_{H^1(\Omega)} \leq C(k,\kappa)H^2(|u|_{H^3(\Omega)} + \|f\|_{L^2(\Omega)}). \tag{4.3}$$

Proof. The proof uses Galerkin orthogonality for the heterogeneous Helmholtz equation, coercivity and continuity of the Helmholtz bilinear form (with k, κ dependence), the multiscale interpolant property, and the triangle inequality.

The MsFEM solution u_H satisfies the Galerkin orthogonality condition for the Helmholtz bilinear form

$$a_{k,\kappa}(u - u_H, v) = 0, \quad \forall v \in U^H, \tag{4.4}$$

where the heterogeneous Helmholtz bilinear form is defined as

$$a_{k,\kappa}(w, v) = \int_\Omega \kappa(\mathbf{x})\nabla w \cdot \nabla v d\mathbf{x} - k^2 \int_\Omega wv d\mathbf{x}, \quad w, v \in H_0^1(\Omega). \tag{4.5}$$

For the Helmholtz equation to be well-posed, we assume the coercivity of $a_{k,\kappa}(\cdot,\cdot)$. There exist constants $\alpha(k,\kappa) > 0$ and $L(k,\kappa) > 0$ such that

$$\alpha(k,\kappa)\|\nabla v\|^2_{L^2(\Omega)} \leq \left|a_{k,\kappa}(v,v)\right|, \quad \forall v \in H_0^1(\Omega),$$

$$\left|a_{k,\kappa}(w,v)\right| \leq L(k,\kappa)\|\nabla w\|_{L^2(\Omega)} \cdot \|\nabla v\|_{L^2(\Omega)}, \quad \forall w, v \in H_0^1(\Omega).$$

Choosing the test function $v = \Pi_H u - u_H$ and substituting it into Eq (4.4), by Galerkin orthogonality, we derive the fundamental error equation for the Helmholtz equation:

$$\begin{aligned} a_{k,\kappa}(\Pi_H u - u_H, \Pi_H u - u_H) &= a_{k,\kappa}(\Pi_H u - u + u - u_H, \Pi_H u - u_H) \\ &= a_{k,\kappa}(\Pi_H u - u, \Pi_H u - u_H). \end{aligned}$$

Applying coercivity and continuity of $a_{k,\kappa}(\cdot,\cdot)$ to both sides, we have

$$\alpha(k,\kappa)\|\Pi_H u - u_H\|^2_{H^1(\Omega)} \leq L(k,\kappa)\|\Pi_H u - u\|_{H^1(\Omega)} \cdot \|\Pi_H u - u_H\|_{H^1(\Omega)}$$

$$\begin{aligned} \Rightarrow \|\Pi_H u - u_H\|_{H^1(\Omega)} &\leq \frac{L(k,\kappa)}{\alpha(k,\kappa)}\|\Pi_H u - u\|_{H^1(\Omega)} && (4.6) \\ &\leq C(k,\kappa)H^2(|u|_{H^3(\Omega)} + \|f\|_{L^2(\Omega)}). && (4.7) \end{aligned}$$

The last step uses Lemma 4.1, and the H^3-seminorm $|u|_{H^3}$ arises from applying a Bramble–Hilbert Lemma argument to the local interpolation error. The dependence on $\|f\|_{L^2}$ enters the analysis due to the coupling of errors across coarse element boundaries or if the source term f has fine-scale structure.

We now relate the error of interest term $\|u_I - u_H\|$ using the triangle inequality,

$$\begin{aligned} \|u_I - u_H\|_{H^1(\Omega)} &\leq \|u_I - \Pi_H u\|_{H^1(\Omega)} + \|\Pi_H u - u_H\|_{H^1(\Omega)} \\ &\leq C_1(k,\kappa)H^2|u|_{H^3(\Omega)} + C_2(k,\kappa)H^2(|u|_{H^3(\Omega)} + \|f\|_{L^2(\Omega)})) \\ &\leq C(k,\kappa)H^2(|u|_{H^3(\Omega)} + \|f\|_{L^2(\Omega)})). \end{aligned}$$

The dependence on $\|f\|_{L^2(\Omega)}$ arises from Helmholtz source term coupling across coarse element boundaries and the fine-scale structure in f. In this derivation, we combine Lemma 4.2 with Eqs (4.6) and (4.7) to establish Lemma 4.3.

Theorem 4.1. The global H^1-error between the exact solution and the multiscale solution of the heterogeneous Helmholtz equation satisfies the second-order superconvergence estimate

$$\|u - u_H\|_{H^1(\Omega)} \leq C(k, \kappa)H^2(|u|_{H^3(\Omega)} + \|f\|_{L^2(\Omega)}) + O(h^2). \tag{4.8}$$

Proof. Applying the triangle inequality for the $H^1(\Omega)$ norm and Lemmas 4.1–4.3, we directly establish the stated result.

It is important to note that linear multiscale basis functions are utilized as the core computational tool in this paper. Given the inherent linearity of these basis functions, the achievement of second-order superconvergence with respect to the H^1 norm is a key highlight in its theoretical results. This property is rarely observed in linear multiscale frameworks, and its realization significantly advances the practical applicability of the proposed method.

5. Numerial results

In this section, the abilities of the proposed multiscale method for solving the Helmholtz equation will be demonstrated. Codes are compiled using Matlab 2020b and run on a desktop computer featuring an Intel Core i9-10900K CPU @ 3.70GHz with 32GB of RAM.

Numerical experiments are conducted to evaluate the respective errors, employing the L^∞ and L^2 norms alongside, most notably, the H^1 norm,

$$\|u - u_H\|_{L^\infty} = \max_{\Omega} |u - u_H|, \tag{5.1}$$

$$\|u - u_H\|_{L^2}^2 = \int_\Omega (u - u_H)^2 \, \mathrm{d}\Omega, \tag{5.2}$$

$$\|u - u_H\|_{H^1}^2 = \int_\Omega \left((u - u_H)^2 + (u - u_H)_x^2 + (u - u_H)_y^2\right) \mathrm{d}\Omega, \tag{5.3}$$

where u_H denotes the multiscale solution on the coarse mesh of size H as given in Eq (3.7). Note that u_H can be replaced by u_g, which represents the Galerkin solution on the fine mesh of size h in Eq (3.3). We compare these numerical solutions with the exact solution u to evaluate the performance of the respective methods. Denote $e = u - u_H$, where the superscripts N and $2N$ refer to the corresponding errors on the coarse and fine meshes, respectively. The convergence order is then computed as

$$\text{order} = \ln\left(\frac{\left\|e^N\right\|}{\left\|e^{2N}\right\|}\right) / \ln 2. \tag{5.4}$$

Example 1. In the Helmholtz equation (2.1), we utilize an exact solution given by

$$u = \sin(\frac{\pi x}{\varepsilon}) \cos(\frac{\pi y}{\varepsilon}), \tag{5.5}$$

with $\varepsilon = 0.1$ chosen to demonstrate the rapid oscillations of the solution; see Figure 1(a). We then introduce a variable wave number $k = \tan(xy)$, a spatially varying coefficient specifically selected to amplify the impact of heterogeneous media. This choice of $k(x, y)$ introduces pronounced spatial variations that mimic real-world heterogeneous environments, thereby enabling a more rigorous

assessment of how the numerical methods perform under conditions where material properties oscillate greatly across the domain. Consequently, the right-hand side force term in the Helmholtz equation is calculated as

$$f = \sin(\frac{\pi x}{\varepsilon})\cos(\frac{\pi y}{\varepsilon})(\frac{2\pi^2}{\varepsilon^2} - k^2).$$

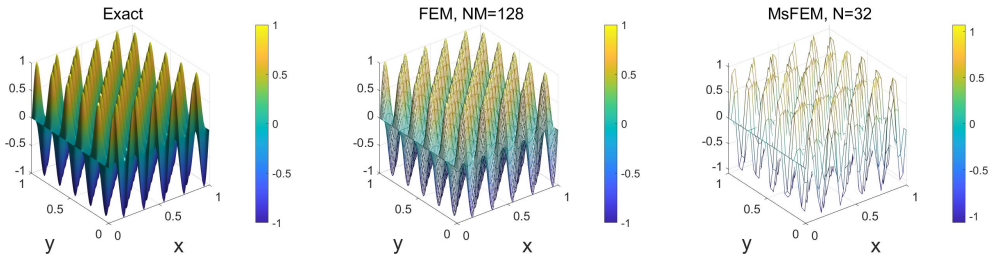

Figure 1. Exact solution, FEM solution on fine mesh ($NM = 128$), and MsFEM solution on coarse mesh ($N = 32$).

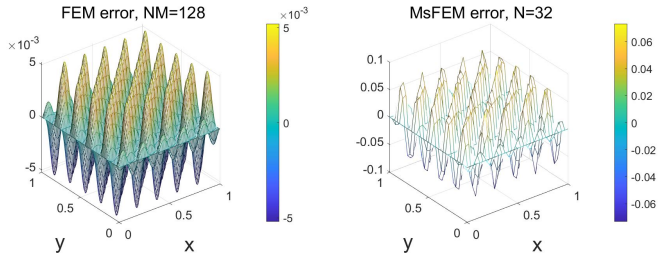

Figure 2. FEM errors on fine mesh ($NM = 128$) and MsFEM errors on coarse mesh ($N = 32$).

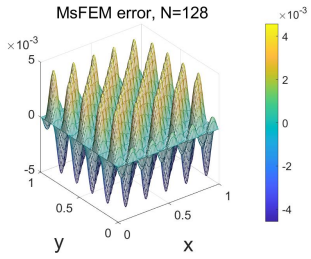

Figure 3. MsFEM errors on fine mesh ($N = 128$).

Note that in solving for the necessary multiscale basis functions within the multiscale approach, we set $M = 4$ in the local problem (3.4). The number M controls the local problem's resolution. Setting $M = 4$ balances accuracy and efficiency, ensuring reliable basis functions without excessive computation. In Figure 1(b),(c), both the FEM solution on the fine mesh number $NM = 128$ and the MsFEM solution on the coarse mesh number $N = 32$ agree well with the exact solution. The corresponding discrete errors are plotted in Figure 2(a),(b). It must be emphasized that, despite the qualitative agreement observed between the two numerical solutions, the error associated with the FEM

solution on the fine mesh is in fact an order of magnitude smaller than that of the MsFEM solution on the coarse mesh. This superior accuracy of the FEM, however, is achieved at the expense of substantially greater computations, encompassing longer simulation runtime and higher memory consumption. This discrepancy underscores the difference between the computational cost and solution accuracy of the two methods. To elaborate further, Figure 3 presents the corresponding MsFEM errors computed on the same fine mesh number $N = 128$. Note that the MsFEM errors are smaller than the FEM errors presented in Figure 2(a).

Table 1. L^∞-norm errors and convergence history of FEM and MsFEM for Example 1.

NM	FEM	order	N	MsFEM	order
16	2.484e-1	-	4	1.004e+0	-
32	7.791e-2	1.67	8	5.616e-1	0.84
64	2.044e-2	1.93	16	2.782e-1	1.01
128	5.203e-3	1.97	32	7.328e-2	1.92
256	1.309e-3	1.99	64	1.821e-2	2.01
512	3.275e-4	2.00	128	4.572e-3	1.99
1024	8.196e-5	2.00	256	1.146e-3	2.00
2048	-	-	512	2.728e-4	2.07

Table 2. L^2-norm errors and convergence history of FEM and MsFEM for Example 1.

NM	FEM	order	N	MsFEM	order
16	5.724e-2	-	4	5.585e-1	-
32	2.996e-2	0.93	8	2.829e-1	0.98
64	8.890e-3	1.75	16	1.437e-1	0.98
128	2.317e-3	1.94	32	4.071e-2	1.82
256	5.855e-4	1.98	64	1.049e-2	1.96
512	1.467e-4	2.00	128	2.643e-3	1.99
1024	3.671e-5	2.00	256	6.620e-4	2.00
2048	-	-	512	1.520e-4	2.12

Tables 1–3 report the numerical error values and the corresponding convergence orders for the FEM and the MsFEM applied to the Helmholtz equation, with the errors measured in the L^∞-norm, L^2-norm, and H^1-norm. Specifically, each table presents the discrete errors obtained by the two methods at different mesh resolutions (characterized by the number of fine/coarse elements, denoted as NM or N in the tables). Notably, for the different configuration (corresponding to the same row in the tables), the multiscale solution yields sufficiently accurate results on a coarse mesh with substantially lower computational resources and time costs. When comparing across different rows, such as when contrasting $N = 512$ with $NM = 512$ (in the FEM) for the same configuration, the multiscale method further exhibits superior numerical accuracy. It is worth emphasizing that, despite its competitive accuracy and wide applicability, the conventional finite element method quickly becomes computationally prohibitive on a single serial computer when used with highly refined meshes (e.g., $NM = 2048$). This reflects a

well-known computational bottleneck that severely restricts its practical performance for large-scale problems. In contrast, the proposed multiscale strategy effectively mitigates this critical drawback, enabling efficient computations even for fine-scale problems while preserving high solution accuracy and numerical stability.

Table 3. H^1-norm errors and convergence history of FEM and MsFEM for Example 1.

NM	FEM	order	N	MsFEM	order
16	2.954e+0	-	4	1.531e+1	-
32	1.385e+0	1.09	8	1.152e+1	0.41
64	3.990e-1	1.80	16	4.323e+0	1.41
128	1.032e-1	1.95	32	1.048e+0	2.04
256	2.603e-2	1.99	64	2.618e-1	2.00
512	6.523e-3	2.00	128	6.549e-2	2.00
1024	1.631e-3	2.00	256	1.637e-2	2.00
2048	-	-	512	4.037e-3	2.02

Example 2. We select an identical exact solution in [12], defined as

$$u(x, y) = \sinh \alpha x \sinh \alpha(\pi - x) \sinh \beta y \sinh \beta(\pi - y). \tag{5.6}$$

Here, we set $\alpha = 1, \beta = 2$, and a large wave number $k = 500$ to embody the challenging high-frequency regime, where the efficient multiscale strategies are critically needed. Consequently, in the Helmholtz equation (2.1), the right-hand force is computed as

$$\begin{aligned} f \;=\; & 2\alpha^2 \cosh \alpha(\pi - 2x) \sinh \beta y \sinh \beta(\pi - y) \\ & +2\beta^2 \cosh \beta(\pi - 2y) \sinh \alpha x \sinh \alpha(\pi - x) \\ & -k^2 \sinh \alpha x \sinh \alpha(\pi - x) \sinh \beta y \sinh \beta(\pi - y). \end{aligned}$$

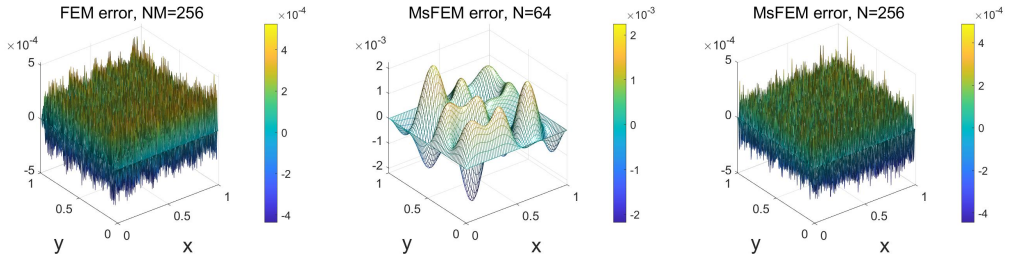

Figure 4. FEM errors on fine mesh ($NM = 256$) and MsFEM errors on coarse meshes with $N = 64$ and $N = 256$.

In Figure 4, we directly show the FEM errors on the fine mesh with the MsFEM errors on the corresponding coarse meshes, clearly visualizing and validating the excellent approximation capability of the proposed MsFEM across different discretization levels.

Table 4. H^1-norm errors and convergence history of FEM and MsFEM for Example 2.

NM	FEM	order	N	MsFEM	order
16	1.676e-2	-	4	1.836e-1	-
32	4.531e-3	1.89	8	3.435e-2	2.42
64	1.179e-3	1.94	16	6.459e-3	2.41
128	3.022e-4	1.96	32	3.148e-3	1.04
256	7.612e-5	1.99	64	9.907e-4	1.67
512	1.919e-5	1.99	128	2.474e-4	2.00
1024	4.758e-6	2.01	256	8.494e-5	1.54
2048	-	-	512	1.876e-5	2.18

Table 4 presents the H^1-norm errors and convergence history of the FEM and MsFEM for Example 2. For brevity, we only report the H^1-norm results here, omitting the L^∞- and L^2-norm data. The FEM results are obtained on fine meshes with $NM = 64, 128, 256, 512$, whereas the MsFEM results are computed on coarse meshes with $N = 64, 128, 256, 512$ at equivalent resolution levels. At these matching nominal resolutions, the MsFEM consistently yields smaller H^1-norm errors on coarse meshes than the FEM does on fine meshes. Moreover, the MsFEM exhibits convergence rates exceeding second-order, confirming theoretical superconvergence.

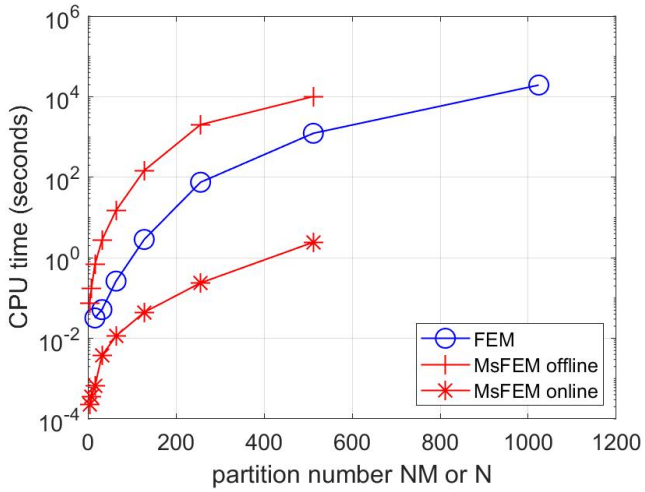

Figure 5. CPU time comparison for Example 2: FEM, MsFEM offline phase, and MsFEM online phase.

Figure 5 quantifies CPU time consumption for the FEM and MsFEM across varying partition numbers to distinguish offline and online costs and validate the efficiency. FEM time represents its total single-stage solution process, growing rapidly with mesh resolution due to full fine-grid stiffness matrix assembly and solving. MsFEM's offline phase includes local basis construction and global mapping matrix assembly, incurring a one-time cost scaling with fine-grid resolution. In contrast, the MsFEM online phase, which performs reduced-order coarse-scale solves using the precomputed global mapping matrix, shows drastically lower CPU time at all resolutions. Even at the largest partition

number, MsFEM online time is several orders of magnitude faster than both FEM total time and MsFEM offline cost. This confirms that the offline precomputation is easily recouped by the efficient online phase, establishing the MsFEM's superiority for large-scale repeated simulations. Notably, such superior accuracy is achieved at a significantly lower computational cost, further validating the MsFEM's effectiveness for large-scale, high-frequency Helmholtz problems.

6. Conclusions

In this work, we have developed a precise, stable, and superconvergent multiscale finite element scheme for the Helmholtz equation in rapidly oscillating heterogeneous media. Based on the scale decomposition of the solution, our multiscale approach achieves both competitive accuracy and remarkable efficiency compared with existing methods. Using linear multiscale basis functions, we rigorously obtain second-order superconvergence in the H^1 norm. Numerical experiments demonstrate that the exact solution exhibits rapid variations along with the large wave numbers, thereby amplifying the heterogeneity of the environment, validating the robust abilities of the proposed multiscale strategy. These results make the MsFEM a practical and reliable approach for solving the Helmholtz equation in various applications such as acoustics, electromagnetics, and wave propagation problems. Inspired by [21, 22], we will further explore more efficient and adaptive multiscale strategies in future research.

Author contributions

Shan Jiang: Methodology, reviewing original draft; Weipeng Miao: Writing original draft; Huayi Wei: Numerical analysis; Nianyu Yi: Validation.

Use of AI tools declaration

The authors declare they have not used Artificial Intelligence (AI) tools in the creation of this article.

Acknowledgments

Supported by NSFC (11771224), China Scholarship Council (CSC) to Shan Jiang, National Key R&D Program of China (2024YFA1012600), NSFC (12371410, 12261131501) to Huayi Wei, NSFC (12431014) to Nianyu Yi. The authors would like to extend our gratitude to the anonymous referees and editors.

Conflict of interest

The authors declare there is no conflict of interest.

References

1. F. Ihlenburg, I. Babuska, Finite element solution of the Helmholtz equation with high wave number. Part I: The *h*-version of the FEM, *Comput. Math. Appl.*, **30** (1995), 9–37. https://doi.org/10.1016/0898-1221(95)00144-N

2. A. A. Oberai, P. M. Pinsky, A multiscale finite element method for the Helmholtz equation, *Comput. Methods Appl. Mech. Eng.*, **154** (1998), 281–297. https://doi.org/10.1016/S0045-7825(97)00130-8

3. I. Babuska, S. A. Sauter, Is the pollution effect of the FEM avoidable for the Helmholtz equation considering high wave numbers? *SIAM J. Numer. Anal.*, **34** (1997), 2392–2423. https://doi.org/10.1137/S0036142994269186

4. D. Gallistl, D. Peterseim, Stable multiscale Petrov-Galerkin finite element method for high frequency acoustic scattering, *Comput. Methods Appl. Mech. Eng.*, **295** (2015), 1–17. https://doi.org/10.1016/j.cma.2015.06.017

5. S. Jiang, M. Presho, Y. Q. Huang, An adapted Petrov-Galerkin multiscale finite element for singularly perturbed reaction-diffusion problems, *Int. J. Comput. Math.*, **93** (2016), 1200–1211. https://doi.org/10.1080/00207160.2015.1041935

6. T. Chaumont-Frelet, On high order methods for the heterogeneous Helmholtz equation, *Comput. Math. Appl.*, **72** (2016), 2203–2225. https://doi.org/10.1016/j.camwa.2016.08.026

7. T. Chaumont-Frelet, F. Valentin, A multiscale hybrid-mixed method for the Helmholtz equation in heterogeneous domains, *SIAM J. Numer. Anal.*, **58** (2020), 1029–1067. https://doi.org/10.1137/19M1255616

8. M. Ohlberger, B. Verfurth, A new heterogeneous multiscale method for the Helmholtz equation with high contrast, *Multiscale Model. Simul.*, **16** (2018), 385–411. https://doi.org/10.1137/16m1108820

9. E. T. Chung, Y. Efendiev, W. T. Leung, Constraint energy minimizing generalized multiscale finite element method, *Comput. Methods Appl. Mech. Eng.*, **339** (2018), 298–319. https://doi.org/10.1016/j.cma.2018.04.010

10. S. B. Fu, K. Gao, R. L. Gibson Jr., E. T. Chung, An efficient high-order multiscale finite element method for frequency-domain elastic wave modeling, *Comput. Geosci.*, **23** (2019), 997–1010. https://doi.org/10.1007/s10596-019-09865-0

11. S. B. Fu, G. L. Li, R. Craster, S. Guenneau, Wavelet-based edge multiscale finite element method for Helmholtz problems in perforated domains, *Multiscale Model. Simul.*, **19** (2021), 1684–1709. https://doi.org/10.1137/19M1267180

12. I. Singer, E. Turkel, Sixth-order accurate finite difference schemes for the Helmholtz equation, *J. Comput. Acoust.*, **14** (2006), 339–351. https://doi.org/10.1142/S0218396X06003050

13. T. T. Wu, R. M. Xu, An optimal compact sixth-order finite difference scheme for the Helmholtz equation, *Comput. Math. Appl.*, **75** (2018), 2520–2537. https://doi.org/10.1016/j.camwa.2017.12.023

14. N. Kumar, R. K. Dubey, A new development of sixth order accurate compact scheme for the Helmholtz equation, *J. Appl. Math. Comput.*, **62** (2020), 637–662. https://doi.org/10.1007/s12190-019-01301-x

15. W. Jiang, X. H. Chen, B. N. Lv, S. S. Jiang, An accurate and efficient multiscale finite-difference frequency-domain method for the scalar Helmholtz equation, *Geophysics*, **87** (2022), T43–T60. https://doi.org/10.1190/GEO2021-0217.1

16. U. Kalachikova, M. Vasilyeva, I. Harris, E. T. Chung, Generalized multiscale finite element method for scattering problem in heterogeneous media, *J. Comput. Appl. Math.*, **424** (2023), 114977. https://doi.org/10.1016/j.cam.2022.114977

17. P. Freese, M. Hauck, D. Peterseim, Super-localized orthogonal decomposition for high-frequency Helmholtz problems, *SIAM J. Sci. Comput.*, **46** (2024), A2377–A2397. https://doi.org/10.1137/21M1465950

18. S. Jiang, A. Protasov, M. L. Sun, Balanced truncation based on generalized multiscale finite element method for the parameter-dependent elliptic problem, *Adv. Appl. Math. Mech.*, **10** (2018), 1527–1548. https://doi.org/10.4208/aamm.OA-2018-0073

19. S. Jiang, Y. Cheng, Y. Cheng, Y. Q. Huang, Generalized multiscale finite element method and balanced truncation for parameter-dependent parabolic problems, *Mathematics*, **11** (2023), 4965. https://doi.org/10.3390/math11244965

20. Y. F. Chen. T. Y. Hou, Y. X. Wang, Exponential convergence for multiscale linear elliptic PDEs via adaptive edge basis functions, *Multiscale Model. Simul.*, **19** (2021), 980–1010. https://doi.org/10.1137/20M1352922

21. Y. F. Chen. T. Y. Hou, Y. X. Wang, Exponentially convergent multiscale methods for 2D high frequency heterogeneous Helmholtz equations, *Multiscale Model. Simul.*, **21** (2023), 849–883. https://doi.org/10.1137/22M1507802

22. Y. F. Chen. T. Y. Hou, Y. X. Wang, Exponentially convergent multiscale finite element method, *Commun. Appl. Math. Comput.*, **6** (2024), 862–878. https://doi.org/10.1007/s42967-023-00260-2

23. S. Jiang, X. Ding, M. L. Sun, Parameter-uniform superconvergence of multiscale computation for singular perturbation exhibiting twin boundary layers, *J. Appl. Anal. Comput.*, **13** (2023), 3330–3351. https://doi.org/10.11948/20230020

24. Y. Cheng, S. Jiang, M. Stynes, Supercloseness of the local discontinuous Galerkin method for a singularly perturbed convection-diffusion problem, *Math. Comput.*, **92** (2023), 2065–2095. https://doi.org/10.1090/mcom/3844

25. Y. Cheng, X. S. Wang, M. Stynes, Optimal balanced-norm error estimate of the LDG method for reaction-diffusion problems I: The one-dimensional case, *J. Sci. Comput.*, **100** (2024), 50. https://doi.org/10.1007/s10915-024-02602-5

26. C. P. Ma, C. Alber, R. Scheichl, Wavenumber explicit convergence of a multiscale generalized finite element method for heterogeneous Helmholtz problems, *SIAM J. Numer. Anal.*, **61** (2023), 1546–1584. https://doi.org/10.1137/21M1466748

27. E. Giammatteo, A. Heinlein, M. Schlottbom, An extension of the approximate component mode synthesis method to the heterogeneous Helmholtz equation, *IMA J. Numer. Anal.*, **45** (2025), 2844–2879. https://doi.org/10.1093/imanum/drae076

28. S. Saini, P. Das, S. Kumar, Parameter uniform higher order numerical treatment for singularly perturbed Robin type parabolic reaction diffusion multiple scale problems with large delay in time, *Appl. Numer. Math.*, **196** (2024), 1–21. https://doi.org/10.1016/j.apnum.2023.10.003

29. D. Sarkar, S. Kumar, P. Das, H. Ramos, Higher-order convergence analysis for interior and boundary layers in a semi-linear reaction-diffusion system networked by a *k*-star graph with non-smooth source terms, *Networks Heterogen. Media*, **19** (2024), 1085–1115. https://doi.org/10.3934/nhm.2024048

30. Y. L. Li, H. J. Wu, Higher-order FEM and CIP-FEM for Helmholtz equation with high wave number and perfectly matched layer truncation, *J. Sci. Comput.*, **104** (2025), 47. https://doi.org/10.1007/s10915-025-02959-1

31. M. Bernkopf, T. Chaumont-Frelet, J. M. Melenk, Wavenumber-explicit stability and convergence analysis of *hp* finite element discretizations of Helmholtz problems in piecewise smooth media, *Math. Comput.*, **94** (2025), 73–122. https://doi.org/10.1090/mcom/3958

AIMS Press